Adjusting Synchronverter Dynamic Response Speed via Damping Correction Loop

Shuan Dong, *Student Member, IEEE*, Yu Christine Chen, *Member, IEEE*

Abstract—This paper proposes to augment the conventional synchronverter control scheme with an auxiliary loop to freely adjust the dynamic response speed. This loop is dubbed as a *damping correction loop* since its form and function are reminiscent of the damping component in the classical synchronous generator model. Central to the proposed auxiliary loop is the creation of an additional tuneable parameter that allows for unrestricted adjustment of the system damping ratio without affecting the steady-state frequency droop characteristic, which is an improvement over the conventional synchronverter design. In the proposed method, relevant parameters are analytically tuned and active- and reactive-power coupling effects are reduced when operating with increased response speed. The dynamic response and robustness of the approach are verified via extensive small-signal analysis. Furthermore, time-domain simulations highlight the advantages of the proposed method over existing ones.

Index Terms—damping correction loop, response speed, synchronverter, transient dynamic response, virtual synchronous generator, voltage source converter.

I. Introduction

THE push toward environmentally responsible electricity generation requires the integration of renewable energy sources (RESs) into the existing power grid. This presents notable challenges in system operations due to the inherent intermittent, variable, and uncertain nature of RESs. As shown in Fig. 1, one way to mitigate these effects is to couple the RES with an energy-storage device, e.g., a battery or a supercapacitor, which acts as a buffer to store surplus energy from the RES or to provide the deficit to the grid, as needed [1], [2]. The energy-storage device can then be connected to the AC network through a voltage source converter (VSC). Thus, with high RES penetration, VSC controller design is of vital importance to ensure that the energy-storage device effectively and efficiently mitigates undesirable effects of RESs.

One way to control VSCs is through the synchronverter [3]– [5], which is a realization of the virtual synchronous generator (VSG) concept [3]–[12]. The basic idea of the synchronverter is to embed the mathematical model of a synchronous generator (SG) along with a simplified governor into the VSC controller so that the VSC behaves like an actual SG and achieves grid frequency regulation. The synchronverter control scheme has several advantages, as follows. First, its operation does not depend on phase-locked loops (PLLs) that are found in conventional VSC control methods, such as vector current control [13] and direct power control [14], which are prone to PLL-related instabilities in weakly-connected networks [15].

S. Dong and Y. C. Chen are with the Department of Electrical and Computer Engineering at the University of British Columbia, Vancouver, BC, V6T 1Z4, Canada. Email: {shuan, chen}@ece.ubc.ca.
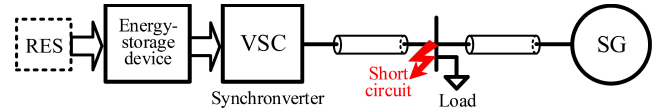
Fig. 1. Illustrative diagram of RES interface with grid.

In this way, the synchronverter is a compelling control strategy for integrating RESs, which are often located in remote areas and connected to a weak grid. Second, by emulating SG rotor dynamics, the synchronverter provides inertia support to the grid and helps to reduce frequency excursions when loads vary or faults occur. This property is highly desirable since the total system inertia diminishes as more RESs replace conventional SGs. Moreover, via its active- and reactive-power control loops, the synchronverter realizes frequency and voltage droop controls in order to improve rotor angle stability and system voltage stability by using only local information [16]. Finally, since the synchronverter is not limited by the physical design of an actual SG [12], embedded parameters can be tuned freely and can even be changed online [10].

Although the synchronverter, as described in [3], operates well under weak grid conditions and contributes inertia support to the grid, one of its major shortcomings is that the dynamic response speed of its active-power loop (APL) cannot be adjusted freely without affecting the steady-state frequency droop characteristic, i.e., the frequency droop coefficient must be modified [5]. Such a modification is undesirable, since the droop coefficient value is fixed by local grid standards [12]. If the APL response speed cannot be tuned and a single-phase-to-earth fault occurs in the grid, as shown in Fig. 1, the synchronverter would not be able to provide timely frequency droop control so as to minimize frequency deviations resulting from the fault. This shortcoming is also evident in other VSG control schemes [8], [12]. In this paper, we propose to add an auxiliary loop in the synchronverter APL so that its response speed can be adjusted freely *without* compromising the steady-state droop characteristic. We name this addition the *damping correction loop*, since its form and function are similar to the damping component in the classical SG model, see, e.g., [17].

Owing to the importance of unrestricted adjustment of the APL dynamic response speed, numerous approaches have been proposed to solve this problem in the literature. In studies on frequency droop control, several methods have been proposed, see, e.g., [18]–[20]. If used directly in synchronverters, however, the transient droop function [18] and the adaptive transient droop function [19] methods induce the undesirable side effect of coupling between the APL and the reactive-

power loop (RPL), and the parameters in the modified droop control law method [20] cannot be analytically tuned to adjust the APL response speed. In studies on VSGs, the alternating inertia control [10] and the virtual impedance method [11] aim to suppress frequency and power oscillations, and as a bonus, also modify the APL response speed. However, the controller in [10] cannot be analytically tuned, and, by adding a virtual impedance, [11] can only *reduce* the APL response speed. On the other hand, the distributed frequency control [21], the differential algorithm [22], and the configurable natural droop controller [23] directly aim to modify the response speed of the APL. However, [21] requires grid frequency measurements from a PLL, which deteriorates this method's effectiveness, especially in weak grid conditions. The differential algorithm in [22] increases the APL response speed by adding a differential term, which may amplify noise in measured signals and result in numerical instability. Finally, the method proposed in [23] induces a zero in the transfer function from the active-power reference value to the active-power output, which may be positive when the APL responds quickly, and thus may cause undesirable non-minimum phase behaviour. Distinct from the methods mentioned above, our proposed method allows for analytical tuning of the APL response speed without using a PLL, producing numerical instability, or causing non-minimum phase behaviour. Moreover, when the APL response speed is increased, our proposed method reduces the coupling between the synchronverter APL and RPL.

Contributions of this paper are as follows. First, we identify the root cause of the synchronverter's shortcoming with transfer function analysis. Next, we propose to add a damping correction loop to the synchronverter APL, which helps to adjust the APL response speed without affecting the steady-state frequency droop characteristic. Finally, we validate the effectiveness of the proposed damping correction loop with small-signal analysis and time-domain simulations.

The remainder of this paper is organized as follows. Section II provides an overview of the conventional synchronverter and identifies its shortcoming. Section III describes the proposed synchronverter with the added damping correction loop. In Sections IV and V, the performance of the proposed synchronverter design is validated through small-signal analysis and time-domain simulations. Finally, concluding remarks and directions for future research are provided in Section VI.

II. PRELIMINARIES

The synchronverter is a power-electronic converter with an SG mathematical model embedded into its controller, so that it emulates SG rotor dynamics and contributes inertia to the grid. The synchronverter consists of active- and reactive-power control loops, among which the APL regulates the active-power output by controlling the virtual rotor speed, thereby adjusting the rotor angle. However, we find that the response speed of the APL cannot be adjusted freely, since to preserve the synchronverter's steady-state frequency droop characteristic, only the inertia constant can be adjusted in the APL. In this section, we provide an overview of the conventional synchronverter and motivate the need to improve the control aimed at unrestricted adjustment of the APL response speed.
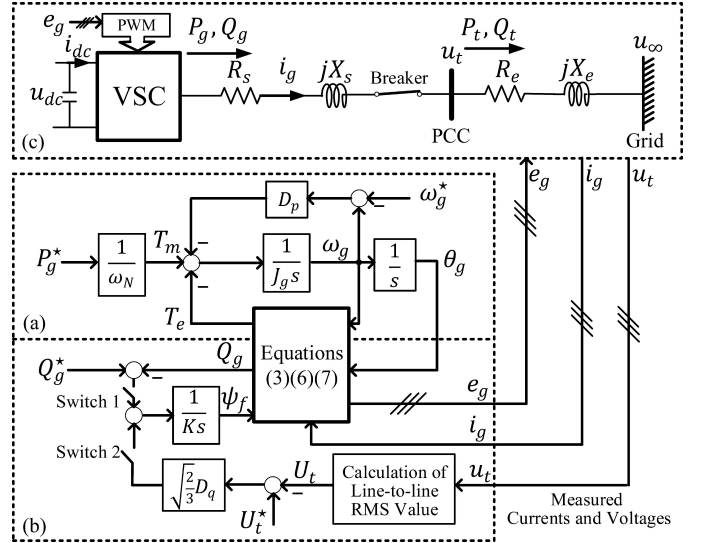
Fig. 2. The conventional synchronverter [3]. (a) synchronverter APL. (b) synchronverter RPL. (c) synchronverter grid interface.

A. Overview of the Conventional Synchronverter

For the SG emulated by the synchronverter control system, assume that (i) it has a round rotor with no damper windings, (ii) there is no flux saturation, (iii) the number of pole-pairs is 1, and (iv) stator windings are star connected with no neutral line. Figure 2 shows a synchronverter-connected system, which consists of the active-power loop (Fig. 2(a)), the reactive-power loop (Fig. 2(b)), and the interface to the grid (Fig. 2(c)). Note that the synchronverter dc-bus voltage u_{dc} is assumed to be constant. Below, with reference to Fig. 2, we explain each component in detail.

1) Active-power Loop: As depicted in Fig. 2(a), the active-power loop (APL) emulates SG rotor dynamics and realizes self synchronization without a PLL. Let ω_g denote the rotating speed of the synchronverter-emulated SG. In order to describe the electromechanical behaviour of the SG, we adopt the standard swing equation, as follows: [17]

$$J_g \frac{d\omega_g}{dt} = T_m - T_e - D_p(\omega_g - \omega_g^\star), \tag{1}$$

where J_g is the inertia constant, T_m is the mechanical input torque, T_e is the electromagnetic torque, and $\omega_g^\star$ is the reference value of ω_g. In (1), the term $-D_p(\omega_g - \omega_g^\star)$ represents a simplified governor with no time delay, so that the synchronverter APL can realize frequency droop control. The frequency droop coefficient, D_p, is determined by

$$D_p = \Delta T_m / \Delta \omega_g, \tag{2}$$

where $\Delta \omega_g = \omega_g - \omega_g^\star$ is the angular speed deviation and ΔT_m is the amount of input torque change required by local grid code [12]. This paper assumes that the torque would change by 100% if the angular speed changes by 0.5% [3].

Let $P_g^\star$ denote the reference value of the synchronverter active-power output P_g; also let ω_N denote the rated angular speed value. Then, in (1), the mechanical input torque is computed as $T_m = P_g^\star / \omega_N$. Additionally, let $i_g = [i_{g\_a}, i_{g\_b}, i_{g\_c}]^\mathrm{T}$ denote the synchronverter stator current; and
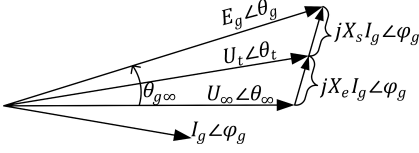
Fig. 3. Phasor diagram of the synchronverter-connected system.

TABLE I
PARAMETERS OF SYNCHRONVERTER-CONNECTED SYSTEM

Parameters	Values	Parameters	Values
R_s	0.741 Ω	L_s	20 mH
R_e	0.0 Ω	L_e	38.5 mH
S_1	1	S_2	0
D_p	1407 $\frac{\text{N} \cdot \text{m} \cdot \text{s}}{\text{rad}}$	J_g	2.814 kg· m^2
D_q	3711 $\frac{\text{Var}}{\text{V}}$	K	27980 $\frac{\text{Var} \cdot \text{rad}}{\text{V}}$
$\omega_N, \omega_g^\star$	376.99 $\frac{\text{rad}}{\text{s}}$	U_∞	6.6 kVrms
rated frequency	60 Hz	rated voltage	6.6 kVrms
rated capacity	1 MVA	DC-link voltage	13 kV

let ψ_f denote the excitation flux obtained from the synchronverter RPL. Then, the electromagnetic torque in (1) is evaluated as [3]

$$T_e = \psi_f i_g^{\mathrm{T}} \left[\sin \theta_g \quad \sin \left(\theta_g - \tfrac{2\pi}{3} \right) \quad \sin \left(\theta_g + \tfrac{2\pi}{3} \right) \right]^{\mathrm{T}}, \quad (3)$$

where the virtual rotor angle $\theta_g = \int_0^t \omega_g \, dt$.

2) Reactive-power Loop: As shown in Fig. 2(b), depending on the states of Switches 1 and 2, the synchronverter reactive-power loop (RPL) regulates its Q_g *or* the line-to-line RMS value U_t of the terminal voltage u_t by adjusting the excitation flux ψ_f. Let S_1 and S_2 represent the states of Switches 1 and 2 ($S_i = 1$ if Switch i is ON, and $S_i = 0$ if Switch i is OFF, $i = 1, 2$). Then, the dynamics of ψ_f are described by

$$K \frac{d\psi_f}{dt} = S_1(Q_g^\star - Q_g) + S_2\sqrt{\frac{2}{3}} \, D_q(U_t^\star - U_t), \quad (4)$$

where K is the control parameter that adjusts the RPL response speed, and $Q_g^\star$ and $U_t^\star$ are reference values for Q_g and U_t. The voltage droop coefficient, D_q, is expressed as

$$D_q = \Delta Q_g / \Delta U_t, \quad (5)$$

where $\Delta U_t = U_t - U_t^\star$ and ΔQ_g is the amount of reactive-power variation required for a commensurate change in U_t, as set by the local grid code [12]. In this paper, Q_g is set to increase 100% if U_t drops 5% [3]. In (4), Q_g obeys [3]

$$Q_g = -\omega_g \psi_f i_g^{\mathrm{T}} \left[\cos \theta_g \quad \cos \left(\theta_g - \tfrac{2\pi}{3} \right) \quad \cos \left(\theta_g + \tfrac{2\pi}{3} \right) \right]^{\mathrm{T}}, \quad (6)$$

which includes the reactive power consumed by the output L-type filter of the synchronverter.

Depending on the states of Switches 1 and 2, the RPL operates under different control modes when used in different application scenarios [4]. For example, in the main grid, with $S_1 = 1$ and $S_2 = 0$, Q-mode supplies the desired reactive power $Q_g^\star$. On the other hand, in microgrid settings, with $S_1 = S_2 = 1$, Q_D-mode is preferred to realize voltage droop control and improve voltage stability. In this paper, Q-mode is adopted for analysis and simulation, but note that this choice has no significant impact on our results.

3) Grid Interface: The final component of the system depicted in Fig. 2 is the synchronverter interface with the grid, which is described here to facilitate our analysis later. The synchronverter inner voltage e_g and its corresponding line-to-line RMS value are, respectively, expressed as

$$e_g = \omega_g \psi_f \left[\sin \theta_g \quad \sin \left(\theta_g - \tfrac{2\pi}{3} \right) \quad \sin \left(\theta_g + \tfrac{2\pi}{3} \right) \right]^{\mathrm{T}}, \quad (7)$$

$$E_g = \sqrt{3/2}\, \omega_g \psi_f, \quad (8)$$

where θ_g is the phase angle of e_g. As depicted in Fig. 2(c), the synchronverter has an output L-type filter with resistance R_s

and reactance X_s, and at the point of common coupling (PCC), it is connected to the grid through a transmission line with resistance R_e and reactance X_e. This paper assumes that the line is predominantly inductive, i.e., $X_e \gg R_e$, and that dynamics of passive components, e.g., inductors, are negligible. Denote the phase angle difference between e_g and the grid voltage u_∞ by $\theta_{g\infty}$ (since $P_g > 0$, $\theta_{g\infty} \in [0, \pi/2]$), which obeys

$$\frac{d\theta_{g\infty}}{dt} = \frac{d\theta_g}{dt} - \frac{d\theta_\infty}{dt} = \omega_g - \omega_\infty, \quad (9)$$

where $\omega_\infty = 2\pi f_\infty$ is the angular speed of u_∞, and θ_∞ is the phase angle of u_∞. Furthermore, denote, by P_t and Q_t, the active and reactive power injected into the grid from the PCC, respectively, so that

$$P_t \approx P_g = \sqrt{\frac{3}{2}} \frac{\omega_g \psi_f U_\infty \sin \theta_{g\infty}}{X_t} =: f_p(\omega_g, \theta_{g\infty}, \psi_f), \quad (10)$$

$$T_e = P_g / \omega_g \approx P_t / \omega_N, \quad (11)$$

$$Q_t = \frac{X_e}{X_t^2} E_g^2 - \frac{X_s}{X_t^2} U_\infty^2 + \frac{X_s - X_e}{X_t^2} E_g U_\infty \cos \theta_{g\infty}$$

$$=: f_q(\omega_g, \theta_{g\infty}, \psi_f), \quad (12)$$

where U_∞ is the line-to-line RMS value of u_∞, and $X_t = X_s + X_e$. According to the geometric relationship highlighted in Fig. 3, the RMS value U_t of terminal voltage u_t is

$$U_t = \sqrt{\frac{X_e^2}{X_t^2} E_g^2 + \frac{X_s^2}{X_t^2} U_\infty^2 + \frac{2X_e X_s}{X_t^2} E_g U_\infty \cos \theta_{g\infty}}$$

$$=: f_u(\omega_g, \theta_{g\infty}, \psi_f). \quad (13)$$

B. Response Speed of the Conventional Synchronverter

As described in Section II-A, the synchronverter APL emulates SG rotor dynamics and realizes frequency droop control. The dynamic behaviour of the APL, as described by (1), can be tuned by varying the inertia J_g as well as the droop coefficient D_p. Next, via a numerical example, we show that only varying J_g does not provide adequate adjustment of the APL response speed. Furthermore, while varying D_p results in modified response speeds, the steady-state droop characteristic is also affected, which is undesirable.

Example 1 (Conventional APL Response Speed)**.** This example uses the system shown in Fig. 2 in conjunction with the relevant parameter values reported in Table I, which are tuned
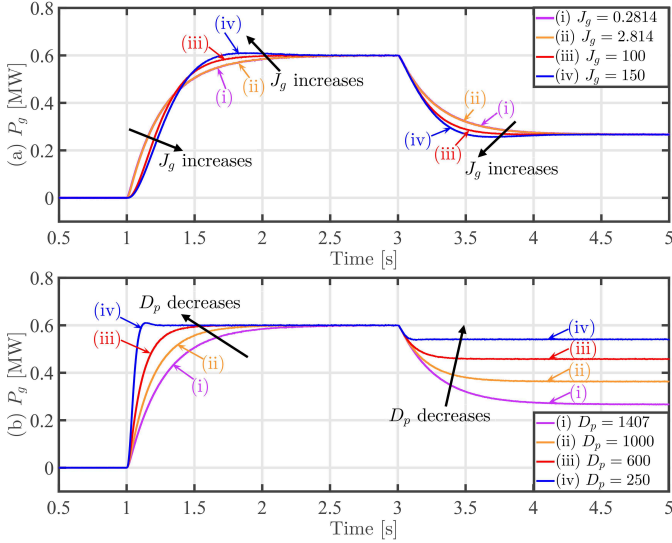
Fig. 4. Transient response of APL when: (a) J_g increases from 0.2814 to 150 ($D_p = 1407$); (b) D_p decreases from 1407 to 250 ($J_g = 2.814$).

according to [3]. In this example, at $t = 0.0$ s, the active- and reactive-power reference values are set to 0, i.e., $P_g^\star = 0$ MW and $Q_g^\star = 0$ MVar, and the grid frequency $f_\infty = 60$ Hz. Then, at $t = 1.0$ s, $P_g^\star$ increases to 0.6 MW while $Q_g^\star$ remains unchanged. Finally, at $t = 3.0$ s, $P_g^\star$ and $Q_g^\star$ remain unchanged, while the grid frequency f_∞ suddenly increases to 60.1 Hz. As evident in Fig. 4(a), even though J_g is varied over the wide range from 0.2814 to 150, no appreciable change in the APL response speed is observed after the events introduced at $t = 1.0$ s and 3.0 s. On the other hand, as shown in Fig. 4(b), decreasing D_p increases the dynamic response speed after the event introduced at $t = 1.0$ s. However, in order to achieve the desired steady-state frequency droop characteristic, D_p should be fixed at 1407. ∎

The phenomena observed in Example 1 can be explained as follows. Consider small variations in APL input variables, $P_g^\star$, ω_∞, $\omega_g^\star$, and ψ_f, denoted by $\Delta P_g^\star$, $\Delta\omega_\infty$, $\Delta\omega_g^\star$, and $\Delta\psi_f$, respectively. Further denote by ΔP_g the variations in the APL output, P_g, resulting from small variations in the input variables. With the above notation in place, linearize (1) and (10) around the equilibrium point (denoted by superscript ∘) and take the Laplace transformation of the resulting small-signal model to obtain the following transfer function:

$$\Delta P_g = G_{11}(s)\Delta P_g^\star + G_{12}(s)\Delta\omega_\infty + G_{13}(s)\Delta\psi_f, \quad (14)$$

where variations in $\omega_g^\star$ are neglected by setting $\Delta\omega_g^\star = 0$. In (14), $G_{11}(s)$ describes dynamics in ΔP_g with respect to $\Delta P_g^\star$, $G_{12}(s)$ reflects the dynamics in ΔP_g with respect to $\Delta\omega_\infty$, and because Q_g is adjusted by ψ_f, $G_{13}(s)$ highlights the influence of the RPL on APL dynamics. The transfer functions $G_{11}(s)$, $G_{12}(s)$, and $G_{13}(s)$ share the same poles and are given by

$$G_{11}(s) = \frac{\omega_{n1}^2}{s^2 + 2\zeta_1\omega_{n1}s + \omega_{n1}^2}, \quad (15)$$

$$G_{12}(s) = \frac{-M \cdot (s + 2\zeta_1\omega_{n1})}{s^2 + 2\zeta_1\omega_{n1}s + \omega_{n1}^2}, \quad (16)$$

$$G_{13}(s) = \frac{N \cdot (s^2 + 2\zeta_1\omega_{n1}s)}{s^2 + 2\zeta_1\omega_{n1}s + \omega_{n1}^2}, \quad (17)$$

respectively, where M and N are expressed as

$$M = \sqrt{\frac{3}{2}} \frac{\omega_N \psi_f^\circ U_\infty \cos\theta_{g\infty}^\circ}{X_t},$$
$$N = \sqrt{\frac{3}{2}} \frac{\omega_N U_\infty \sin\theta_{g\infty}^\circ}{X_t}, \quad (18)$$

respectively. In (15)–(17), the damping ratio ζ_1 and the natural frequency ω_{n1} are given by

$$\zeta_1 = \left(\sqrt{\frac{X_t}{2\sqrt{6}\psi_f^\circ U_\infty \cos\theta_{g\infty}^\circ}}\right) \cdot \frac{D_p}{\sqrt{J_g}},$$
$$\omega_{n1} = \left(\sqrt{\sqrt{\frac{3}{2}}\frac{\psi_f^\circ U_\infty \cos\theta_{g\infty}^\circ}{X_t}}\right) \cdot \frac{1}{\sqrt{J_g}}, \quad (19)$$

respectively. We present detailed derivation of (14)–(17) in Appendix A. Note that, in (19), both ζ_1 and ω_{n1} are inversely proportional to $\sqrt{J_g}$. Hence, reducing J_g results in larger ζ_1, which causes the system to be over damped and to respond slowly. Conversely, increasing J_g results in smaller ω_{n1}, which limits the system bandwidth and still makes the APL respond slowly. Thus, as shown in Fig. 4(a), tuning only J_g cannot satisfy both ζ_1 and ω_{n1} design requirements and consequently cannot adjust the APL response speed effectively. On the other hand, as shown in Fig. 4(b) and deduced from (19), the response speed can be adjusted by varying D_p, as decreasing D_p reduces ζ_1 but does not influence ω_{n1}. In this case, however, the steady-state frequency droop characteristic is not preserved, i.e., P_g decreases less when f_∞ increases to 60.1 Hz. This is undesirable as the droop coefficient D_p is set to a particular value based on local grid code to enhance stability [12].

In summary, the response speed of the conventional synchronverter APL cannot be adequately adjusted without affecting the steady-state droop characteristic. As described above, the root cause is that tuning only one parameter J_g cannot simultaneously satisfy both ζ_1 and ω_{n1} design requirements. In the next section, we aim to adjust the response speed of the APL without affecting the desired droop characteristic.

III. PROPOSED SYNCHRONVERTER CONTROLLER DESIGN

Targeted at unrestricted adjustment of the APL dynamic response speed, this section proposes a damping correction loop to be added into the existing APL. With the augmented controller in place, we show that the response speed of the improved synchronverter can be adjusted freely *without* affecting its steady-state frequency droop characteristic. A block diagram of the proposed synchronverter controller, including both the APL and the RPL, is shown in Fig. 5, which is interfaced with the grid as in Fig. 2(c).

In order to focus on the core idea behind the proposed damping correction loop, for now, neglect all first-order low-pass filters (LPFs) in Fig. 5. In other words, even though T_{ef} and ψ_{ff} are obtained by filtering T_e and ψ_f signals with LPFs, for now assume that $T_{ef} \approx T_e$ and $\psi_{ff} \approx \psi_f$ (we will return to these filters in a later discussion). The inputs to the damping
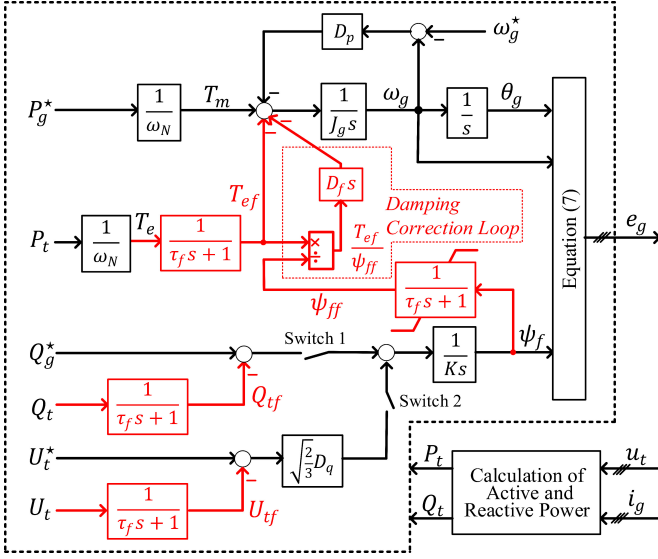
Fig. 5. Proposed synchronverter controller with damping correction loop.

correction loop are T_{ef} and ψ_{ff}, and its output is $D_f \frac{d}{dt}\left(\frac{T_{ef}}{\psi_{ff}}\right)$, where D_f [V·s²/rad] is a tuneable parameter. After adding this loop into the existing APL, (1) becomes

$$J_g \frac{d\omega_g}{dt} = T_m - T_{ef} - D_p(\omega_g - \omega_g^\star) - D_f \frac{d}{dt}\left(\frac{T_{ef}}{\psi_{ff}}\right). \quad (20)$$

With the proposed damping correction loop in place, we make two key observations. First, note that the steady-state value of the additional term $D_f \frac{d}{dt}\left(\frac{T_{ef}}{\psi_{ff}}\right)$ in (20) is exactly zero. As a direct consequence, D_p remains as the original droop coefficient, and the desired steady-state frequency droop characteristic is preserved. Second, during the transient period prior to reaching steady state, the additional term $D_f \frac{d}{dt}\left(\frac{T_{ef}}{\psi_{ff}}\right)$ acts to modify the APL damping. This is evident by substituting (10) into (11) and further the resultant expression into $D_f \frac{d}{dt}\left(\frac{T_{ef}}{\psi_{ff}}\right)$ to obtain

$$D_f \frac{d}{dt}\left(\frac{T_{ef}}{\psi_{ff}}\right) \approx \left(D_f \sqrt{\frac{3}{2}} \frac{U_\infty \cos\theta_{g\infty}}{X_t}\right) \cdot (\omega_g - \omega_\infty), \quad (21)$$

where $T_{ef} \approx T_e$ and $\psi_{ff} \approx \psi_f$ are implicitly assumed.

To illustrate how the damping correction loop influences the APL response speed, analogous to the analysis conducted in Section II-B, consider small variations in the same input variables $\Delta P_g^\star$, $\Delta\omega_\infty$, and $\Delta\psi_f$. Here, we define the system output as P_t (instead of P_g in the original synchronverter) as this is the actual active power injected into the grid. Denote by ΔP_t variations in P_t resulting from small variations $\Delta P_g^\star$, $\Delta\omega_\infty$, and $\Delta\psi_f$. Then, by linearizing (10) and (20) around the equilibrium point and applying the Laplace transformation on the resulting small-signal model, we obtain the following transfer function:

$$\Delta P_t = G_{21}(s)\Delta P_g^\star + G_{22}(s)\Delta\omega_\infty + G_{23}(s)\Delta\psi_f, \quad (22)$$

where

$$G_{21}(s) = \frac{\omega_{n2}^2}{s^2 + 2\zeta_2\omega_{n2}s + \omega_{n2}^2}, \quad (23)$$

$$G_{22}(s) = \frac{-M \cdot (s + 2\zeta_1\omega_{n2})}{s^2 + 2\zeta_2\omega_{n2}s + \omega_{n2}^2}, \quad (24)$$

$$G_{23}(s) = \frac{N \cdot (s^2 + 2\zeta_2\omega_{n2}s)}{s^2 + 2\zeta_2\omega_{n2}s + \omega_{n2}^2}, \quad (25)$$

M and N are given by (18), and the damping ratio ζ_2 and the natural frequency ω_{n2} are expressed as

$$\zeta_2 = \left(\sqrt{\frac{X_t}{2\sqrt{6}\psi_f^\circ U_\infty \cos\theta_{g\infty}^\circ}}\right) \cdot \frac{D_p + D_f\sqrt{\frac{3}{2}}\frac{U_\infty \cos\theta_{g\infty}^\circ}{X_t}}{\sqrt{J_g}},$$

$$\omega_{n2} = \omega_{n1}, \quad (26)$$

respectively. In the augmented APL, according to (26), the natural frequency ω_{n2} can be tuned by J_g, as described in Section II-B. At the same time, the damping ratio ζ_2 can be independently adjusted by tuning D_f. For example, with $\theta_{g\infty}^\circ \in [0,\ \pi/2]$, $\zeta_2 = \zeta_1$ if $D_f = 0$, $\zeta_2 > \zeta_1$ if $D_f > 0$, and $\zeta_2 < \zeta_1$ if $D_f < 0$. Thus, by introducing an additional degree of freedom to the original APL controller, the proposed damping correction loop allows ζ_2 and ω_{n2} design requirements to be satisfied simultaneously.

Remark 1 (Connection to Transient Droop Function [18]). While myriad other schemes have been proposed in the literature, we comment on the connection between our method and the so-called "transient droop function" method since it boils down to augmenting the swing equation in (1) with a derivative term and is thus most closely related to the method proposed in this paper. Specifically, the method in [18] is equivalent to augmenting (1) so that it becomes

$$J_g \frac{d\omega_g}{dt} = T_m - T_{ef} - D_p(\omega_g - \omega_g^\star) - D_m \frac{dP_t}{dt}. \quad (27)$$

Via a similar exercise as the one done to obtain (14), we get

$$\Delta P_t = G_{31}(s)\Delta P_g^\star + G_{32}(s)\Delta\omega_\infty + G_{33}(s)\Delta\psi_f. \quad (28)$$

It is straightforward to show that setting $D_m = D_f/(\omega_N\psi_f^\circ)$ results in $G_{31}(s) = G_{21}(s)$, $G_{32}(s) = G_{22}(s)$, and

$$G_{33}(s) = \frac{N \cdot (s^2 + 2\zeta_1\omega_{n2}s)}{s^2 + 2\zeta_2\omega_{n2}s + \omega_{n2}^2}. \quad (29)$$

Since $G_{21}(s) = G_{31}(s)$ and $G_{22}(s) = G_{32}(s)$, both the proposed damping correction loop and the transient droop function lead to the same dynamic performance in ΔP_t with respect to $\Delta P_g^\star$ and $\Delta\omega_\infty$. However, with increased APL dynamic response speed, the transient droop function strengthens the coupling between the APL and the RPL. To see this, consider the case in which J_g is reduced to increase the bandwidth of the APL, in an effort to increase the synchronverter response speed. According to (19), however, this causes ζ_1 to increase, creating an over-damped system. In order to increase the response speed, the core idea in both the proposed damping correction loop and the transient droop function is to reduce the damping ratio independently, by tuning D_f in the former method and D_m in the latter. Recall that $G_{23}(s)$ and $G_{33}(s)$ isolate the impact of the RPL on the APL in the two methods, and the only difference between $G_{23}(s)$ and $G_{33}(s)$ is in the coefficients multiplying s in the numerators, namely, $2N\zeta_2\omega_{n2}$ in (25) and $2N\zeta_1\omega_{n2}$

in (29). As $\zeta_1 > \zeta_2$ and $N > 0$ for $\theta_{g\infty}^{\circ} \in [0, \ \pi/2]$, we have that $2N\zeta_1\omega_{n2} > 2N\zeta_2\omega_{n2}$. Consequently, if ψ_f is increased to supply more reactive power, for the same $\Delta\psi_f > 0$, $G_{33}(s)\Delta\psi_f$ would imply a larger temporary rise in ΔP_t than $G_{23}(s)\Delta\psi_f$. In this way, the transient droop function strengthens the coupling between the APL and the RPL. So comparatively, for fast APL response, the proposed damping correction loop achieves the desired dynamic performance with reduced active- and reactive-power coupling. ∎

Remark 2 (Realizing Self Synchronization)**.** For the synchronverter, synchronization is the ability to closely track its internal voltage e_g to u_t, and hence to the grid voltage u_∞, prior to closing the breaker in Fig. 2(c) [4]. Synchronization helps to minimize start-up currents when the VSC becomes physically connected to the grid. To avoid the need for a dedicated synchronization unit and to simplify the controller, a desirable synchronverter feature is to have self-synchronization capability, i.e., the ability to synchronize the VSC with the grid before connecting them *without* a PLL [4]. In order to achieve self synchronization, the synchronverter must be able to (i) operate in P-mode in which P_t tracks $P_g^\star$ without steady-state error and Q-mode with both $P_g^\star$ and $Q_g^\star$ set to zero, and (ii) via a virtual impedance branch, compute virtual currents and feed them back into the controller [4]. These features ensure that $e_g \approx u_t$ before the VSC is physically connected to the grid, and thus enable the synchronverter to realize synchronization and reduce start-up currents immediately after breaker closure. The proposed controller design is equipped to achieve the features mentioned above and, in turn, self synchronization. First, with reference to Fig. 2(c), before closing the breaker, the synchronverter can operate in P-mode with the damping torque supplied only by the damping correction loop (i.e., set $D_p = 0$). Also, as described in Section II-A2, the RPL can operate in Q-mode with switches $S_1 = 1$ and $S_2 = 0$. The current i_g that feeds back into the controller in Fig. 5 is computed by having the difference $(e_g - u_t)$ pass through a virtual impedance branch $(L_v s + R_v)^{-1}$, where L_v and R_v are tuned by trial and error. Finally, both active- and reactive-power reference values $P_g^\star$ and $Q_g^\star$ are set to zero during the self-synchronization process prior to breaker closure. In this way, our design satisfies both features (i) and (ii) above and thus achieves self synchronization. ∎

In addition to the damping correction loop, there are two minor differences between the conventional and proposed synchronverter designs. First, in the RPL, first-order LPFs are implemented to smooth ψ_f, T_e, Q_t, and U_t. The smoothed

signals are ψ_{ff}, T_{ef}, Q_{tf}, and U_{tf}, respectively, where

$$\tau_f \frac{d\psi_{ff}}{dt} = -\psi_{ff} + \psi_f, \quad \tau_f \frac{dT_{ef}}{dt} = -T_{ef} + T_e,$$
$$\tau_f \frac{dQ_{tf}}{dt} = -Q_{tf} + Q_t, \quad \tau_f \frac{dU_{tf}}{dt} = -U_{tf} + U_t, \quad (30)$$

with $T_e = P_t/\omega_N$, and P_t, Q_t, and U_t are, respectively, given by (10), (12), and (13). Note that all filter time constants are assumed to be equal, and their impacts are studied in Section IV. Furthermore, Q_{tf} (instead of Q_g in the original synchronverter) is used as the feedback signal, as it reflects the actual reactive power (after being filtered) injected into the grid. Thus, the dynamics of ψ_f obey

$$K\frac{d\psi_f}{dt} = S_1(Q_g^\star - Q_{tf}) + S_2\sqrt{\frac{2}{3}}\, D_q(U_t^\star - U_{tf}). \quad (31)$$

During normal operation, parameters in the proposed synchronverter controller are tuned as follows. Statuses of Switches 1 and 2 are chosen based on the application scenario as discussed in Section II-A. The droop coefficients, D_p and D_q, are set by the local grid code. The parameter K can be chosen based on the method described in [3]. Finally, τ_f, J_g, and D_f can be tuned using small-signal analysis, which is detailed next.

IV. SMALL-SIGNAL ANALYSIS

In Section III, the synchronverter with the proposed damping correction loop is described, but the impacts of the first-order LPFs are neglected. In this section, we include these LPFs and develop the full small-signal state-space model of the synchronverter-connected system linearized around the equilibrium point. To this end, the dynamics of synchronverter-connected system with the proposed controller are fully described by (9), (20), (30), and (31). Linearize these around the equilibrium point $\boldsymbol{x}^\circ$ to obtain the following small-signal state-space model:

$$\frac{d\Delta\boldsymbol{x}}{dt} = \boldsymbol{A}\Delta\boldsymbol{x} + \boldsymbol{B}\Delta\boldsymbol{u}, \quad (32)$$

where the state vector $\Delta\boldsymbol{x}$ and input vector $\Delta\boldsymbol{u}$ are

$$\Delta\boldsymbol{x} = [\Delta\omega_g, \Delta\theta_{g\infty}, \Delta\psi_f, \Delta\psi_{ff}, \Delta T_{ef}, \Delta Q_{tf}, \Delta U_{tf}]^{\mathrm{T}},$$
$$\Delta\boldsymbol{u} = [\Delta P_g^\star, \Delta Q_g^\star, \Delta U_t^\star, \Delta\omega_g^\star, \Delta\omega_\infty]^{\mathrm{T}}, \quad (33)$$

respectively. With reference to Fig. 2(c) and Fig. 5, these state variables are selected since they are obtained by integration and remain constant in steady state. Note that we choose $\theta_{g\infty}$ rather than θ_g because $\theta_{g\infty}$ is constant in steady state while θ_g varies as its derivative ω_g is not zero. Moreover, P_t, T_e, Q_t,

$$\boldsymbol{A} = \begin{bmatrix} -\sqrt{\frac{3}{2}}\frac{D_f U_\infty \sin\theta_{g\infty}^\circ}{J_g \tau_f \omega_N X_t} - \frac{D_p}{J_g} & -\sqrt{\frac{3}{2}}\frac{D_f \omega_g^\circ U_\infty \cos\theta_{g\infty}^\circ}{J_g \tau_f \omega_N X_t} & \frac{D_f(X_t \omega_N T_{ef}^\circ - \sqrt{\frac{3}{2}}\omega_g^\circ U_\infty \psi_{ff}^\circ \sin\theta_{g\infty}^\circ)}{J_g(\psi_{ff}^\circ)^2 \tau_f \omega_N X_t} & \frac{-D_f T_{ef}^\circ}{J_g(\psi_{ff}^\circ)^2 \tau_f} & \frac{D_f - \psi_{ff}^\circ \tau_f}{J_g \psi_{ff}^\circ \tau_f} & 0 & 0 \\ 1 & 0 & 0 & 0 & 0 & 0 & 0 \\ 0 & 0 & 0 & 0 & 0 & \frac{-S_1}{K} & -\sqrt{\frac{2}{3}}\frac{S_2 D_q}{K} \\ 0 & 0 & \frac{1}{\tau_f} & \frac{-1}{\tau_f} & 0 & 0 & 0 \\ \sqrt{\frac{3}{2}}\frac{\psi_f^\circ U_\infty \sin\theta_{g\infty}^\circ}{\tau_f \omega_N X_t} & \sqrt{\frac{3}{2}}\frac{\omega_g^\circ \psi_f^\circ U_\infty \cos\theta_{g\infty}^\circ}{\tau_f \omega_N X_t} & \sqrt{\frac{3}{2}}\frac{\omega_g^\circ U_\infty \sin\theta_{g\infty}^\circ}{\tau_f \omega_N X_t} & 0 & \frac{-1}{\tau_f} & 0 & 0 \\ \frac{1}{\tau_f}\left(\frac{\partial f_q}{\partial\omega_g}\right)|_{\boldsymbol{x}^\circ} & \frac{1}{\tau_f}\left(\frac{\partial f_q}{\partial\theta_{g\infty}}\right)|_{\boldsymbol{x}^\circ} & \frac{1}{\tau_f}\left(\frac{\partial f_q}{\partial\psi_f}\right)|_{\boldsymbol{x}^\circ} & 0 & 0 & \frac{-1}{\tau_f} & 0 \\ \frac{1}{\tau_f}\left(\frac{\partial f_u}{\partial\omega_g}\right)|_{\boldsymbol{x}^\circ} & \frac{1}{\tau_f}\left(\frac{\partial f_u}{\partial\theta_{g\infty}}\right)|_{\boldsymbol{x}^\circ} & \frac{1}{\tau_f}\left(\frac{\partial f_u}{\partial\psi_f}\right)|_{\boldsymbol{x}^\circ} & 0 & 0 & 0 & \frac{-1}{\tau_f} \end{bmatrix} \quad (\dagger)$$
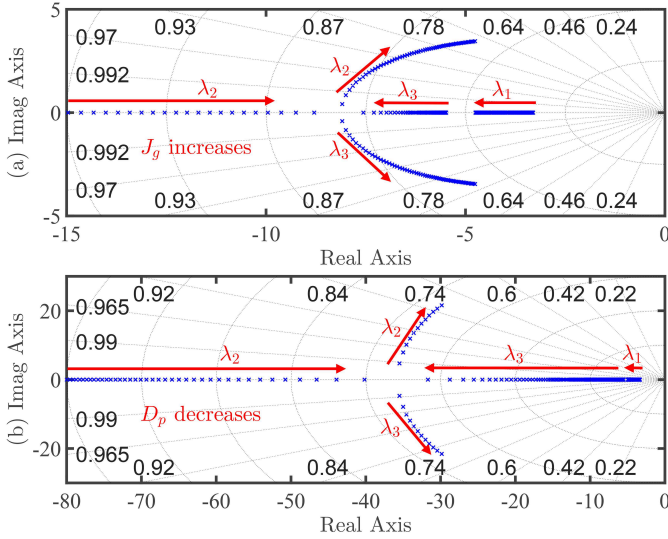
Fig. 6. Dominant modes of improved synchronverter *without* the damping correction loop. (a) J_g increases from 0.2814 to 150 ($D_f = 0$, $\tau_f = 0.01$, $P_t = 0.6$ MW, $Q_t = 0$ MVar). (b) D_p decreases from 1407 to 250 ($D_f = 0$, $\tau_f = 0.01$, $P_t = 0.6$ MW, $Q_t = 0$ MVar).

and U_t in (30) are all functions of $\theta_{g\infty}$ according to (10)–(13). The state matrix $\boldsymbol{A}$ is shown in (†), while the input matrix $\boldsymbol{B}$ is omitted due to space constraints. In Appendix B, the linearized model developed in (32) is verified against the nonlinear model dynamics.

The matrix $\boldsymbol{A}$ has 7 eigenvalues, denoted by $\lambda_k, k = 1, ..., 7$. As the LPFs in (30) are considered in (32), this model accurately describes the small-signal dynamic behaviour of the synchronverter. With the model in (32), we conduct eigenvalue sensitivity analysis to validate the effectiveness of the proposed controller design and highlight its robustness against operating-point changes. Using participation-factor analysis, we find that the state ΔT_{ef} is closely related to eigenvalues λ_2 and λ_3, so we focus on these in the analysis below. For the impact of the proposed damping correction loop on the other eigenvalues, please refer to Appendix C.

1) Without Damping Correction Loop: Let $D_f = 0$, so that the dynamic performance of the synchronverter without the damping correction loop can be examined. Figure 6(a) shows that when J_g increases, the two real poles λ_2 and λ_3 meet and split into complex-conjugate poles, i.e., the damping ratio ζ_2 of the APL decreases. However, their magnitudes $|\lambda_2|$ and $|\lambda_3|$ decrease, i.e., increasing J_g reduces the natural frequency ω_{n2}. Thus, only tuning J_g cannot place this pair of eigenvalues further away from the imaginary axis and cannot adjust the APL response speed freely. Figure. 6(b) shows that varying D_p changes the APL damping ratio, but has negligible influence $|\lambda_2|$ and $|\lambda_3|$. As the original APL is over damped, reducing D_p makes λ_3 move towards the left and increases the APL response speed, but this affects the steady-state frequency droop characteristic as explained in Section II.

2) With Damping Correction Loop: Here, allow D_f to be an additional tuneable parameter. Figure 7(a) shows that, by decreasing D_f, the two real poles λ_2 and λ_3 meet and become two complex-conjugate poles, and thereafter $|\lambda_2|$
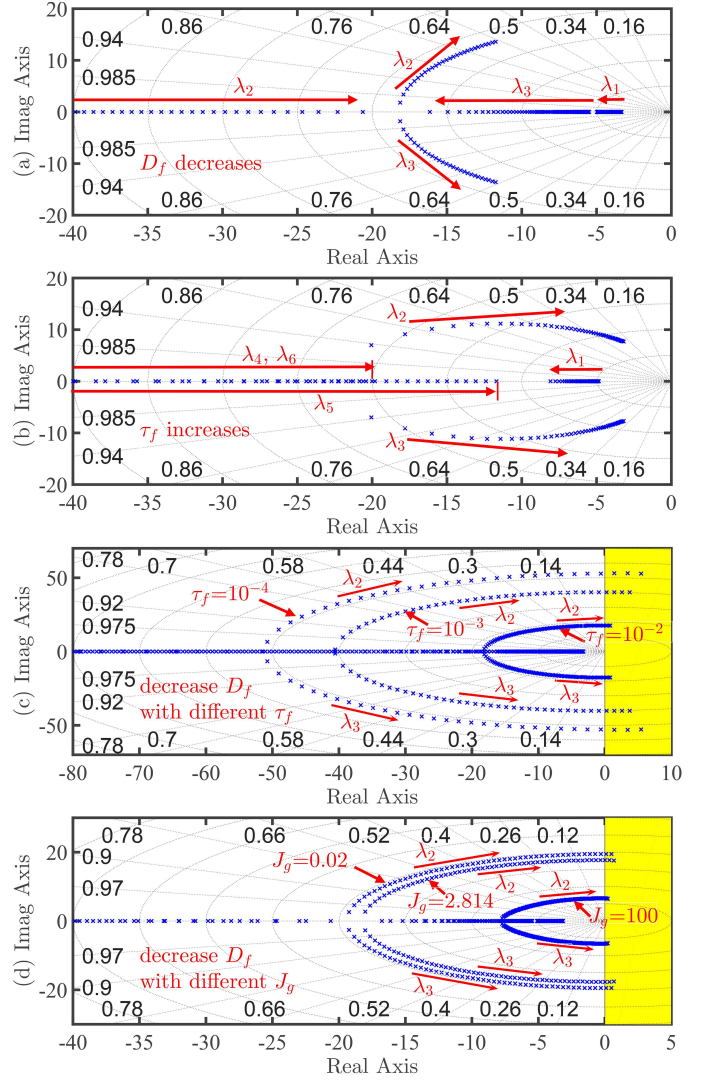
Fig. 7. Dominant modes of improved synchronverter *with* the damping correction loop. (a) D_f decreases from 0 to -3 ($\tau_f = 0.01$, $P_t = 0.6$ MW, $Q_t = 0$ MVar). (b) τ_f increases from 0.007 to 0.05 ($D_f = -2.76$, $P_t = 0.6$ MW, $Q_t = 0$ MVar). (c) D_f decreases from 0 to -4.1 when τ_f respectively takes 0.01, 0.001, and 0.0001 ($P_t = 0.6$ MW, $Q_t = 0$ MVar). (d) D_f decreases from 0.2 to -4.1 when J_g respectively takes 0.02, 2.814, 100 ($\tau_f = 0.01$, $P_t = 0.6$ MW, $Q_t = 0$ MVar).

and $|\lambda_3|$ remain unchanged. Thus, as (26) predicts, tuning D_f adjusts the damping ratio ζ_2 without affecting the natural frequency ω_{n2}. Next, Fig. 7(b) shows that increasing τ_f not only reduces the damping ratio ζ_2, but also makes the natural frequency ω_{n2} smaller.

Figures 7(c) and 7(d) show two families of root loci when D_f varies with different τ_f and J_g. We observe that if τ_f or J_g becomes smaller, the natural frequency ω_{n2} would increase. It is worth noting that there are mutual influences between τ_f and J_g. For example, if τ_f takes the value of 0.01 s, as shown in Fig. 7(d), a larger J_g would reduce ω_{n2} significantly, while a smaller J_g would only increase ω_{n2} slightly. Also, there is a tradeoff between the first-order LPFs' filtering ability and the APL dynamic performance, i.e., while reducing τ_f increases ω_{n2}, it also reduces the LPFs' noise rejection ability.
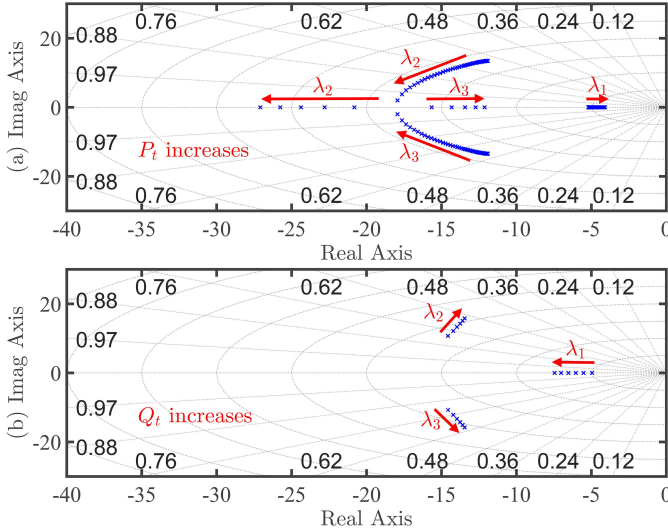
Fig. 8. Dominant modes of improved synchronverter when validating the robustness of the proposed design. (a) P_t increases from 0 to 1 MW ($D_f = -2.76$, $\tau_f = 0.01$, $Q_t = 0$ MVar). (b) Q_g increases from 0 to 0.8 MVar ($D_f = -2.76$, $\tau_f = 0.01$, $P_t = 0$ MW).

The analysis above shows that, with the proposed damping correction loop, and by simultaneously tuning D_f, J_g and τ_f, eigenvalues λ_2 and λ_3 can be placed more freely, and the degrees of freedom in the controller are increased.

3) Robustness of Proposed Design: Figure 8(a) shows that when the synchronverter active-power output P_t increases from 0 MW to 1 MW, the damping ratio ζ_2 increases accordingly. On the other hand, Fig. 8(b) shows that an increase in the reactive-power output Q_t from 0 MVar to 0.8 MVar only causes ζ_2 to decrease slightly. In this way, the proposed controller is robust against variations in the operating point.

V. SIMULATION RESULTS

In this section, via time-domain simulations, we not only validate the effectiveness of the proposed damping correction loop during normal operation, but also verify that the proposed design realizes self synchronization. The simulated system consists of the proposed synchronverter controller shown in Fig. 5 and its interface to the grid shown in Fig. 2(c). The synchronverter-connected system is modelled in PSCAD/EMTDC, with $\tau_f = 0.01$ s and other parameter values reported in Table I, unless otherwise noted.

A. During Normal Operation

In this case study, at $t = 1.0$ s, $P_g^\star$ increases from 0 MW to 0.6 MW, and at $t = 3.0$ s, the grid frequency f_∞ increases from 60.0 Hz to 60.1 Hz. As shown in Fig. 9(a), decreasing D_f reduces the damping ratio of the synchronverter APL as (26) predicts. Since the original APL is over damped, a smaller D_f causes the APL to respond more quickly. By setting $D_f = -2.76$ V·s²/rad, the APL damping ratio $\zeta_2 \approx 0.8$, and satisfactory transient response speed is obtained, as illustrated in Fig. 9(a). With ζ_2 held at 0.8 by adjusting D_f, increasing J_g causes the synchronverter APL to respond more
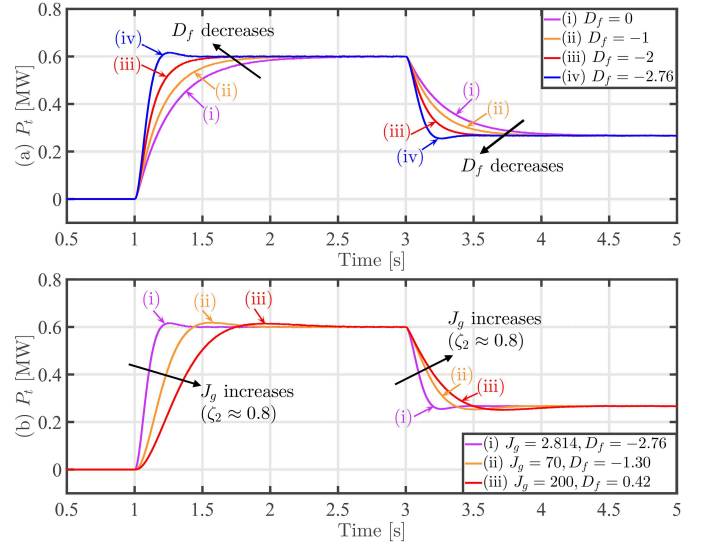
Fig. 9. Transient response of APL when: (a) D_f decreases from 0 to -2.76 ($J_g = 2.814$). (b) J_g increases from 2.814 to 200 ($\zeta_2 \approx 0.8$).
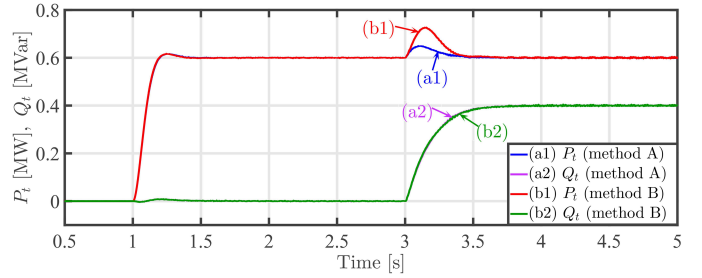
Fig. 10. Comparison between damping correction loop (method A) and transient droop function (method B).

slowly, as shown in Fig. 9(b). This is due to the decreased bandwidth as predicted by (19) and (26). We note that the steady-state frequency droop characteristic is preserved in both Figs. 9(a) and 9(b).

Remark 3 (Comparison with Transient Droop Function [18])**.** To ensure a fair comparison, the transient droop function (method B) is tuned so that it has the same dynamic response as the proposed damping correction loop method (method A) with respect to variations in $P_g^\star$. As shown in Fig. 10, following the increase in $P_g^\star$ from 0 MW to 0.6 MW at $t = 1.0$ s, traces (a1) and (b1), corresponding to the dynamic response of P_t in methods A and B, respectively, are identical. At $t = 3.0$ s, $Q_g^\star$ increases from 0 MVar to 0.4 MVar. After this event, traces (a2) and (b2) in Fig. 10, corresponding to the dynamic response of Q_t in methods A and B, respectively, are identical, since the same value of K is chosen for both methods. Q_t is increased by making ψ_f larger, and P_t is influenced by ψ_f (note that this influence is discussed in detail in Remark 1), so at $t = 3.0$ s, P_t traces in both methods A and B rise temporarily. As shown in Fig. 10, the transient induced in method A is much smaller than that in method B. We conclude that, with high APL response speeds, the proposed damping correction loop method significantly diminishes the coupling between the APL and the RPL. ■
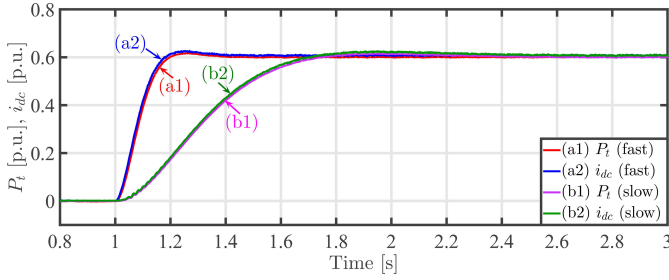
Fig. 11. Impact of the damping correction loop on dc-side current when the APL response is fast ($J_g = 2.814$, $D_f = -2.76$) and slow ($J_g = 200$, $D_f = 0.42$).

Remark 4 (Impact on dc-side Current). The proposed damping correction loop influences the dynamics of the ac-side output power, P_t, as observed in Fig. 9. As a side effect, the dynamics of the dc-side current i_{dc} are also affected, because the dc side of the synchronverter transfers power to the ac side, as shown in Fig. 2(c). To examine the effect of the damping correction loop on i_{dc}, we consider two cases: (i) APL responds quickly with $J_g = 2.814 \text{ kg} \cdot \text{m}^2$ and $D_f = -2.76 \text{ V} \cdot \text{s}^2/\text{rad}$, and (ii) APL responds slowly with $J_g = 200 \text{ kg} \cdot \text{m}^2$ and $D_f = 0.42 \text{ V} \cdot \text{s}^2/\text{rad}$. In Fig. 11, we adopt per-unit quantities for $P_g^\star$, P_t, and i_{dc} to promote ease of comparison. During the simulations, at $t = 1.0$ s, $P_g^\star$ increases from 0 to 0.6 p.u. (i.e., 0.6 MW). As shown in Fig. 11, traces (a1) and (a2), respectively corresponding to P_t and i_{dc} when the APL responds quickly, are nearly identical. Similarly, traces (b1) and (b2), corresponding to the case of slow APL response, are nearly identical. These observations are explained as follows. Referring to Fig. 2(c), suppose losses in the VSC as well as the L-type filter resistance R_s are neglected, we have that $P_t \approx u_{dc}i_{dc}$. And since the dc-side voltage u_{dc} is fixed at its rated value (or in per-unit quantities, $u_{dc} = 1$ p.u.), then indeed, $P_t \approx i_{dc}$ in per-unit quantities, as shown in Fig. 11. From the above, we conclude that the impact of the proposed damping correction loop on the ac-side output power and the dc-side current are nearly identical in per-unit quantities (and they are directly proportional to each other in actual quantities with fixed u_{dc}). ∎

B. Realizing Self Synchronization

Via time-domain simulations, we validate the proposed self-synchronization method described in Remark 2. In this case study, the grid frequency $f_\infty = 60.1$ Hz, $\tau_f = 0.01$ s, the virtual impedance branch is set to $(0.05s + 10)^{-1}$ (tuned by trial and error). All parameters except D_p are reported in Table I. Prior to physically connecting the VSC to the grid, i.e., closing the breaker in Fig. 2(c), the synchronverter is synchronized to the grid. Then, the breaker is closed and normal operation, as validated in Section V-A, begins. With reference to simulation results shown in Fig. 12, at $t = 0.0$ s, the synchronverter operates in P-mode (with $D_p = 0 \text{ N} \cdot \text{m} \cdot \text{s/rad}$ and $D_f = 1.00 \text{ V} \cdot \text{s}^2/\text{rad}$) and Q-mode (with $S_1 = 1$ and $S_2 = 0$), where $P_g^\star = 0$ MW and $Q_g^\star = 0$ MVar. As an example, Fig. 12(b) shows that the synchronverter a-phase inner voltage e_{g_a} converges to the grid voltage u_{t_a}
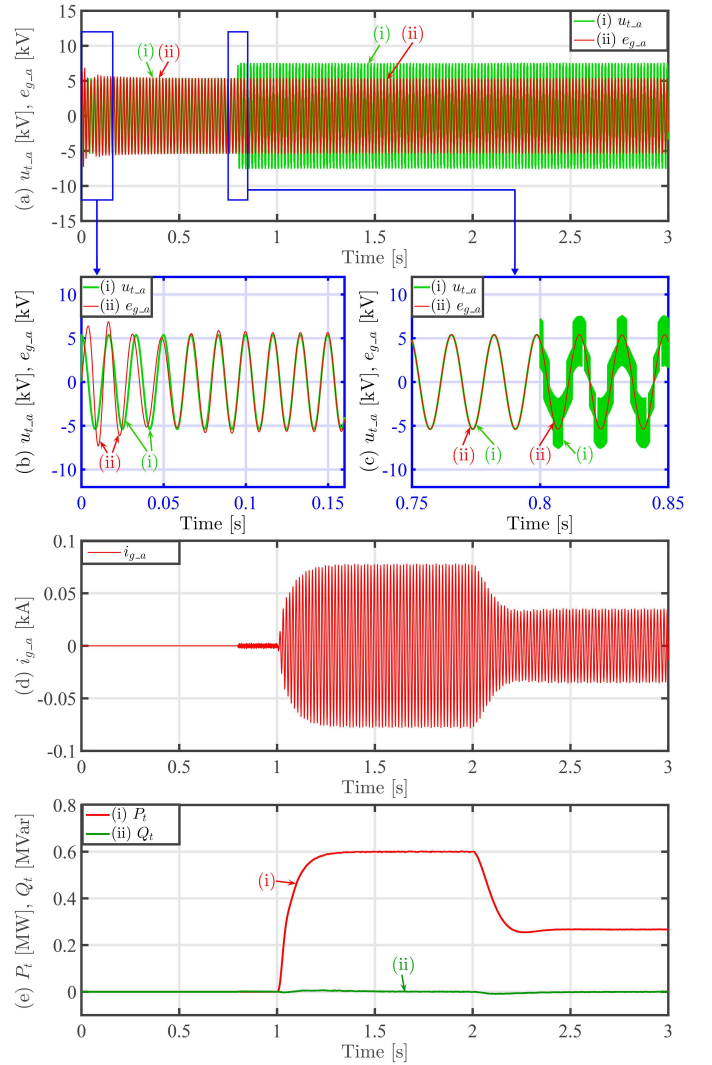
Fig. 12. Self-synchronization process of improved synchronverter with the damping correction loop when $f_\infty = 60.1$ Hz.

(note that $u_t = u_\infty$ before the breaker is closed) within 0.15 s. When the breaker is closed at $t = 0.8$ s and normal operation (as depicted in Fig. 5) begins, self synchronization is achieved with $e_{g\_a} \approx u_{t\_a}$, as shown in Fig. 12(c). Moreover, Fig. 12(d) shows that there is no significant surge current after closing the breaker. (Note that in Fig. 12(c), the harmonics in u_{t_a} after $t = 0.8$ s are caused by fast switching devices, and an LCL-type filter can be included to filter them out. As this issue is not the focus of this paper, we refrain from dwelling on it further.) At $t = 1.0$ s, the active-power reference value $P_g^\star$ increases from 0.0 to 0.6 MW. Since the frequency droop controller is inactive (i.e., $D_p = 0$), the active-power output P_t tracks $P_g^\star$ to 0.6 MW even though the grid frequency $f_\infty = 60.1$ Hz. Finally, at $t = 2.0$ s, the frequency droop controller is activated with $D_p = 1407 \text{ N} \cdot \text{m} \cdot \text{s/rad}$, and the damping correction loop is reset with $D_f = -2.76 \text{ V} \cdot \text{s}^2/\text{rad}$. As shown in Fig. 12(e), the synchronverter soon decreases its active-power output automatically to regulate the grid frequency. To close this discussion, we note that the results shown in Fig. 12 are typical and, in general, our proposed design achieves self synchronization regardless of the initial grid frequency.

VI. Concluding Remarks

This paper identifies a shortcoming in the synchronverter in that its APL lacks in control degrees of freedom, and thus is unable to adjust its dynamic response speed freely. To mitigate this problem, we propose to add a damping correction loop to the synchronverter APL, which allows the response speed to be adjusted freely without affecting the steady-state frequency droop characteristic. Moreover, the coupling between the APL and the RPL is reduced when the APL is tuned to respond quickly. Compelling directions for future work include leveraging the proposed design for applications in SVGs, HVDC links, and wind power integration. Since the proposed controller modifies the synchronverter damping ratio, another relevant application that can be tackled is that of power system stabilizers, where one attempts to damp system oscillations in order to help stabilize the grid.

Appendix

A. Derivation of Transfer Functions (14)–(17)

We begin with the swing equation of the original synchronverter, i.e., (1), in which the mechanical input torque $T_m = P_g^\star/\omega_N$, and according to (10) and (11), the electromagnetic torque T_e is expressed as

$$T_e = \frac{P_g}{\omega_g} = \sqrt{\frac{3}{2}}\frac{\psi_f U_\infty \sin\theta_{g\infty}}{X_t}. \tag{34}$$

Substituting these expressions for T_m and T_e into (1), we get that

$$J_g\frac{d\omega_g}{dt} = \frac{P_g^\star}{\omega_N} - \sqrt{\frac{3}{2}}\frac{\psi_f U_\infty \sin\theta_{g\infty}}{X_t} - D_p(\omega_g - \omega_g^\star). \tag{35}$$

As for ω_g, it can be obtained from (9) as

$$\omega_g = \frac{d\theta_{g\infty}}{dt} + \omega_\infty. \tag{36}$$

Then, take the derivative of (36) to get

$$\frac{d\omega_g}{dt} = \frac{d^2\theta_{g\infty}}{dt^2} + \frac{d\omega_\infty}{dt}. \tag{37}$$

Next, we substitute (36) and (37) into (35) to get

$$J_g\left(\frac{d^2\theta_{g\infty}}{dt^2} + \frac{d\omega_\infty}{dt}\right) = \frac{P_g^\star}{\omega_N} - \sqrt{\frac{3}{2}}\frac{\psi_f U_\infty \sin\theta_{g\infty}}{X_t} \\ - D_p\left(\left(\frac{d\theta_{g\infty}}{dt} + \omega_\infty\right) - \omega_g^\star\right). \tag{38}$$

Then, as described in Section II-B, consider small variations in the APL input variables $P_g^\star$, ω_∞, and ψ_f ($\omega_g^\star$ remains unchanged), and denote these small variations as $\Delta P_g^\star$, $\Delta\omega_\infty$, and $\Delta\psi_f$, respectively. Linearizing (38) around the equilibrium point (denoted by superscript $\circ$), we have that

$$J_g\left(\frac{d^2\Delta\theta_{g\infty}}{dt^2} + \frac{d\Delta\omega_\infty}{dt}\right) = \frac{\Delta P_g^\star}{\omega_N} - \sqrt{\frac{3}{2}}\frac{U_\infty}{X_t}\left(\sin\theta_{g\infty}^\circ\Delta\psi_f \\ + \psi_f^\circ\cos\theta_{g\infty}^\circ\Delta\theta_{g\infty}\right) - D_p\left(\frac{d\Delta\theta_{g\infty}}{dt} + \Delta\omega_\infty\right), \tag{39}$$

where $\Delta\theta_{g\infty}$ denotes small variations in $\theta_{g\infty}$ arising from $\Delta P_g^\star$, $\Delta\omega_\infty$, and $\Delta\psi_f$. Next, by taking the Laplace

transformation of (39), we get (while mildly abuse notation by using the same symbols for both time- and s-domain variables)

$$J_g\left(s^2\Delta\theta_{g\infty} + s\Delta\omega_\infty\right) = \frac{\Delta P_g^\star}{\omega_N} - \sqrt{\frac{3}{2}}\frac{U_\infty}{X_t}\left(\sin\theta_{g\infty}^\circ\Delta\psi_f \\ + \psi_f^\circ\cos\theta_{g\infty}^\circ\Delta\theta_{g\infty}\right) - D_p\left(s\Delta\theta_{g\infty} + \Delta\omega_\infty\right). \tag{40}$$

Solving (40) for $\Delta\theta_{g\infty}$, we get

$$\Delta\theta_{g\infty} = \frac{\frac{\Delta P_g^\star}{\omega_N} - (J_g s + D_p)\Delta\omega_\infty - \sqrt{\frac{3}{2}}\frac{U_\infty\sin\theta_{g\infty}^\circ}{X_t}\Delta\psi_f}{J_g s^2 + D_p s + \sqrt{\frac{3}{2}}\frac{\psi_f^\circ U_\infty\cos\theta_{g\infty}^\circ}{X_t}}. \tag{41}$$

Next, consider small variations in the APL output P_g expressed in (10), resulting from small variations in the input variables, and linearize (10) with respect to ω_g, $\theta_{g\infty}$, and ψ_f by taking appropriate partial derivatives to arrive at a small-signal model. It turns out that $\frac{\partial P_g}{\partial\omega_g}|_{\boldsymbol{x}^\circ}$ is much smaller than $\frac{\partial P_g}{\partial\psi_f}|_{\boldsymbol{x}^\circ}$ and $\frac{\partial P_g}{\partial\theta_{g\infty}}|_{\boldsymbol{x}^\circ}$, so we neglect the $\frac{\partial P_g}{\partial\omega_g}|_{\boldsymbol{x}^\circ}\Delta\omega_g$ term in ΔP_g. Assuming that $\omega_g^\circ = \omega_N$, the small-signal output variable ΔP_g can be expressed as

$$\Delta P_g = \sqrt{\frac{3}{2}}\frac{\omega_N U_\infty}{X_t}\left(\sin\theta_{g\infty}^\circ\Delta\psi_f + \psi_f^\circ\cos\theta_{g\infty}^\circ\Delta\theta_{g\infty}\right). \tag{42}$$

Finally, by substituting (41) into (42) and defining M, N, ζ_1 and ω_{n1} as in (18) and (19), the transfer functions (14)–(17) are obtained, as desired.

B. Verification of Linearized Model

In this section, we verify the small-signal state-space model used in Section IV, similar to the method discussed in [24]. First, we recognize P_t and Q_t as system output variables, resulting in the output vector $\boldsymbol{y} = [P_t, Q_t]^\mathrm{T}$. Next, consider sufficiently small perturbations in $\boldsymbol{y}$, denoted by $\Delta\boldsymbol{y}$ and linearize output equations (10) and (12) to get

$$\Delta\boldsymbol{y} = \boldsymbol{C}\Delta\boldsymbol{x} + \boldsymbol{D}\Delta\boldsymbol{u}, \tag{43}$$

where $\Delta\boldsymbol{x}$ and $\Delta\boldsymbol{u}$ are described in (33), and $\boldsymbol{C}$ and $\boldsymbol{D}$ are computed by appropriately taking partial derivatives of $f_p(\omega_g, \theta_{g\infty}, \psi_f)$ and $f_q(\omega_g, \theta_{g\infty}, \psi_f)$ in (10) and (12), respectively, and evaluating for a fixed operating point. Note that $\boldsymbol{D} = \boldsymbol{0}$ since $f_p(\omega_g, \theta_{g\infty}, \psi_f)$ and $f_q(\omega_g, \theta_{g\infty}, \psi_f)$ do not depend on any input variables. In order to verify the linearized model, which consists (32) and (43), against the nonlinear synchronverter-connected system modelled in PSCAD/EMTDC, we conduct time-domain simulations and compare the dynamic response of the two models. Both models use parameter values reported in Table I, $D_f = -2.76\ \mathrm{V\cdot m^2/rad}$, and $\tau_f = 0.01\ \mathrm{s}$. The linearized model is obtained by linearizing the nonlinear system around the equilibrium point corresponding to $P_t = 0.6\ \mathrm{MW}$ and $Q_t = 0.0\ \mathrm{MVar}$.

Simulation results are displayed in Fig. 13, in which cases (i) (blue trace) and (ii) (red trace), respectively, represent the active-power output P_t obtained from the nonlinear and linearized models. Beginning at $t = 0.5$ s, the active-power reference value $P_g^\star = 0.6$ MW, the reactive-power reference
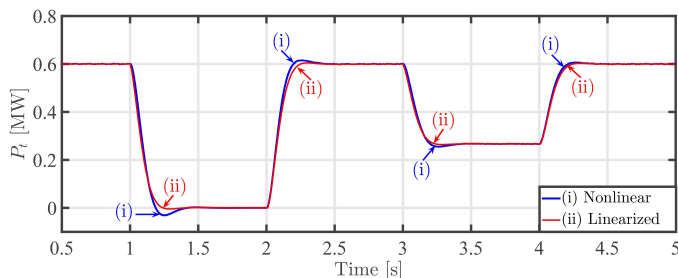
Fig. 13. Verification of the linearized small-signal state-space model.

TABLE II
EIGENVALUE SENSITIVITIES TO PARAMETER D_f

	Value of λ_k, $k = 1, ..., 7$	Sensitivity of λ_k to D_f (i.e., $\frac{\partial \lambda_k}{\partial D_f}$)	Impact of increasing D_f
λ_1	$-4.9433 + j0.0000$	$0.13161 - j0.0000$	Re(λ_1) ↗
λ_2	$-14.556 + j10.723$	$-11.840 - j15.304$	Re(λ_2) ↘, Im(λ_2) ↘
λ_3	$-14.556 - j10.723$	$-11.840 + j15.304$	Re(λ_3) ↘, Im(λ_3) ↗
λ_4	$-100.00 + j0.0000$	$-0.0000 + j0.0000$	
λ_5	$-94.800 + j0.0000$	$0.0059503 + j0.0000$	Re(λ_5) ↗
λ_6	$-100.00 + j0.0000$	$0.0000 + j0.0000$	
λ_7	$-541.72 + j0.0000$	$12.884 + j0.0000$	Re(λ_7) ↗

value $Q_t^\star = 0$ MVar, the grid frequency $f_\infty = 60$ Hz, and the synchronverter operates in steady state. Then, at $t = 1.0$ s, $P_g^\star$ decreases from 0.6 MW to 0 MW. After this disturbance, from Fig. 13, we note that the dynamic response of the nonlinear model has a larger overshoot than that of the linearized one. This is reasonable because the synchronverter operating point is moved away from the linearization point, and according to Fig. 8, a smaller P_t corresponds to a smaller damping ratio ζ_2. Based on this, we expect that the nonlinear model would have a slightly larger overshoot when $P_g^\star$ becomes 0 MW. For the remainder of the simulation, at $t = 2.0$ s, $P_g^\star$ increases from 0 MW to 0.6 MW, and at $t = 3.0$ s, f_∞ increases from 60 Hz to 60.1 Hz, and then decreases from 60.1 Hz to 60 Hz at $t = 4.0$ s. Following each of these disturbances, the dynamic response resulting from the nonlinear and linearized models are well matched.

Based on the simulation results shown in Fig. 13, we conclude that the dynamic behaviour of the nonlinear model is sufficiently mimicked by the linearized model composed of (32) and (43), thus verifying its $\boldsymbol{A}$ matrix to be used to tune design parameters as done in Section IV.

C. Impact of Damping Correction Loop on Eigenvalues

In this section, we systematically evaluate the impact of the proposed damping correction loop on all eigenvalues of the linearized system and conclude that indeed, this loop mainly influences λ_2 and λ_3, to which, as stated in Section IV, ΔT_{ef} is most closely related. To assess these influences, we first note that studying the impact of the damping correction loop on the eigenvalues is equivalent to studying the impact of varying the parameter D_f. The influence of the parameter D_f on the eigenvalue λ_k can be quantitatively determined by computing the sensitivity of each eigenvalue to D_f, as follows: [17]

$$\frac{\partial \lambda_k}{\partial D_f} = \frac{\boldsymbol{q}_k^\mathrm{T} \left[\frac{\partial \boldsymbol{A}}{\partial D_f}\right] \boldsymbol{p}_k}{\boldsymbol{q}_k^\mathrm{T} \boldsymbol{p}_k}, \tag{44}$$

where $\boldsymbol{q}_k$ is the left eigenvector of the state matrix $\boldsymbol{A}$ (see (†)) corresponding to λ_k (i.e., $\boldsymbol{q}_k^\mathrm{T} \boldsymbol{A} = \lambda_k \boldsymbol{q}_k^\mathrm{T}$), and $\boldsymbol{p}_k$ is the right eigenvector of $\boldsymbol{A}$ corresponding to λ_k (i.e., $\boldsymbol{A}\boldsymbol{p}_k = \lambda_k \boldsymbol{p}_k$).

For the sensitivity analysis, we assume that the synchronverter-connected system parameters are as in Table I, $D_f = -2.76$ V·s²/rad, and $\tau_f = 0.01$ s. Linearizing the system around the operating point $P_t = 0.6$ MW and $Q_t = 0.0$ MVar, and using (44), we compute the sensitivity of each eigenvalue to the parameter D_f, the results

from which are summarized in Table II (Re(λ_k) and Im(λ_k) represent the real and imaginary parts of λ_k, respectively). We find that other than λ_2 and λ_3, the damping correction loop also influences λ_1, λ_5, and λ_7. Specifically, λ_1, λ_5, and λ_7 would increase as D_f increases. However, from Table II, we note that the magnitudes of sensitivities $\left|\text{Re}(\frac{\partial \lambda_2}{\partial D_f})\right| = 11.840$ and $\left|\text{Im}(\frac{\partial \lambda_2}{\partial D_f})\right| = 15.304$ are comparable to the magnitude of the eigenvalue itself $\left|\lambda_2\right| = 18.079$, and this is also true for λ_3. On the other hand, for λ_1, λ_5, and λ_7, $\left|\text{Re}(\frac{\partial \lambda_k}{\partial D_f})\right| \ll \left|\lambda_k\right|$ and $\left|\text{Im}(\frac{\partial \lambda_k}{\partial D_f})\right| \ll \left|\lambda_k\right|$, $k = 1, 5, 7$. For example, $\left|\text{Re}(\frac{\partial \lambda_7}{\partial D_f})\right| = 12.884 \ll \left|\lambda_7\right| = 541.72$. Based on this reasoning, we conclude that the damping correction loop influences λ_2 and λ_3 more than λ_1, λ_5, and λ_7.

It is worth noting that although the eigenvalue sensitivity analysis above only evaluates the impact of D_f on λ_k with one set of parameters, it can be repeated under other operating conditions, with D_f taking other values. The repeated analysis reveals similar trends in that λ_2 and λ_3 are influenced more than other eigenvalues. Detailed results from this are omitted here to avoid repetition.

REFERENCES

[1] G. Delille, B. Francois, and G. Malarange, "Dynamic frequency control support by energy storage to reduce the impact of wind and solar generation on isolated power system's inertia," *IEEE Trans. Sustain. Energy*, vol. 3, no. 4, pp. 931–939, Oct. 2012.
[2] N. W. Miller. (2014, Jan. 23) GE experience with turbine integrated battery energy storage. [Online]. Available: http://www.ieee-pes.org/presentations/gm2014/PESGM2014P-000717.pdf
[3] Q.-C. Zhong and G. Weiss, "Synchronverters: Inverters that mimic synchronous generators," *IEEE Trans. Ind. Electron.*, vol. 58, no. 4, pp. 1259–1267, Apr. 2011.
[4] Q.-C. Zhong, P. L. Nguyen, Z. Ma, and W. Sheng, "Self-synchronized synchronverters: Inverters without a dedicated synchronization unit," *IEEE Trans. Power Electron.*, vol. 29, no. 2, pp. 617–630, Feb. 2014.
[5] R. Aouini, B. Marinescu, K. B. Kilani, and M. Elleuch, "Synchronverter-based emulation and control of hvdc transmission," *IEEE Trans. Power Syst.*, vol. 31, no. 1, pp. 278–286, Jan. 2016.
[6] H. P. Beck and R. Hesse, "Virtual synchronous machine," in *Proc. 9th Int. Conf. EPQU*, 2007, pp. 1–6.
[7] F. Gao and M. R. Iravani, "A control strategy for a distributed generation unit in grid-connected and autonomous modes of operation," *IEEE Trans. Power Del.*, vol. 23, no. 2, pp. 850–859, Apr. 2008.
[8] M. Ashabani and Y.-R. Mohamed, "Novel comprehensive control framework for incorporating VSCs to smart power grids using bidirectional synchronous-VSC," *IEEE Trans. Power Syst.*, vol. 29, no. 2, pp. 943–957, Mar. 2014.

[9] S. D'Arco and J. A. Suul, "Virtual synchronous machines-classification of implementations and analysis of equivalence to droop controllers for microgrids," in *Proc. IEEE PowerTech Grenoble*, 2013, pp. 1–7.

[10] J. Alipoor, Y. Miura, and T. Ise, "Power system stabilization using virtual synchronous generator with alternating moment of inertia," *IEEE J. Emerg. Sel. Topics Power Electron.*, vol. 3, no. 2, pp. 451–458, Jun. 2015.

[11] J. Liu, Y. Miura, H. Bevrani, and T. Ise, "Enhanced virtual synchronous generator control for parallel inverters in microgrids," *IEEE Trans. Smart Grid*, to be published.

[12] H. Wu, X. Ruan, D. Yang, X. Chen, W. Zhao, Z. Lv, and Q.-C. Zhong, "Small-signal modeling and parameters design for virtual synchronous generators," *IEEE Trans. Ind. Electron.*, vol. 63, no. 7, pp. 4292–4303, Jul. 2016.

[13] A. Yazdani and R. Iravani, *Voltage-sourced converters in power systems: modeling, control, and applications.* NJ: Wiley, 2010.

[14] T. Noguchi, H. Tomiki, S. Kondo, and I. Takahashi, "Direct power control of pwm converter without power-source voltage sensors," *IEEE Trans. Ind. Appl.*, vol. 34, no. 3, pp. 473–479, May/Jun. 1998.

[15] D. Dong, B. Wen, D. Boroyevich, P. Mattavelli, and Y. Xue, "Analysis of phase-locked loop low-frequency stability in three-phase grid-connected power converters considering impedance interactions," *IEEE Trans. Ind. Electron.*, vol. 62, no. 1, pp. 310–321, Jan. 2015.

[16] M. C. Chandorkar, D. M. Divan, and R. Adapa, "Control of parallel connected inverters in standalone ac supply systems," *IEEE Trans. Ind. Appl.*, vol. 29, no. 1, pp. 136–143, Jan./Feb. 1993.

[17] P. Kundur, N. J. Balu, and M. G. Lauby, *Power system stability and control.* New York: McGraw-hill, 1994.

[18] J. M. Guerrero, L. G. de Vicuna, J. Matas, M. Castilla, and J. Miret, "A wireless controller to enhance dynamic performance of parallel inverters in distributed generation systems," *IEEE Trans. Power Electron.*, vol. 19, no. 5, pp. 1205–1213, Sep. 2004.

[19] Y. A.-R. I. Mohamed and E. F. El-Saadany, "Adaptive decentralized droop controller to preserve power sharing stability of paralleled inverters in distributed generation microgrids," *IEEE Trans. Power Electron.*, vol. 23, no. 6, pp. 2806–2816, Nov. 2008.

[20] N. Soni, S. Doolla, and M. C. Chandorkar, "Improvement of transient response in microgrids using virtual inertia," *IEEE Trans. Power Del.*, vol. 28, no. 3, pp. 1830–1838, Jul. 2013.

[21] Y. Du, J. M. Guerrero, L. Chang, J. Su, and M. Mao, "Modeling, analysis, and design of a frequency-droop-based virtual synchronous generator for microgrid applications," in *Proc. IEEE ECCE Asia Downunder*, 2013, pp. 643–649.

[22] H. Xu, X. Zhang, F. Liu, F. Miao, R. Shi, and H. Ni, "An improved virtual synchronous generator algorithm for system stability enhancement," in *Proc. IEEE 2nd Int. Future Energy Electron. Conf.*, 2015, pp. 1–6.

[23] W. Zhang, A. Cantarellas, J. Rocabert, A. Luna, and P. Rodriguez, "Synchronous power controller with flexible droop characteristics for renewable power generation systems," *IEEE Trans. Sustain. Energy*, to be published.

[24] S. D'Arco, J. A. Suul, and M. Molinas, "Implementation and analysis of a control scheme for damping of oscillations in vsc-based hvdc grids," in *Power Electronics and Motion Control Conf. and Expo. (PEMC)*, Sep. 2014, pp. 586–593.